

Driving and characterizing nucleation of urea and glycine polymorphs in water

Ziyue Zou^{a,†}, Eric R. Beyerle^{b,†}, Sun-Ting Tsai^b, and Pratyush Tiwary^{a,c,1}

^aDepartment of Chemistry and Biochemistry, University of Maryland, College Park, MD 20742; ^bDepartment of Physics, University of Maryland, College Park, MD 20742;

^cInstitute for Physical Science and Technology, University of Maryland, College Park, MD 20742

Crystal nucleation is relevant across the domains of fundamental and applied sciences. However, in many cases its mechanism remains unclear due to a lack of temporal or spatial resolution. To gain insights to the molecular details of nucleation, some form of molecular dynamics simulations are typically performed, which are, in turn, limited by their ability to run long enough to sample the nucleation event thoroughly. To overcome the timescale limits in typical molecular dynamics simulations in a manner free of prior human bias, here we employ the machine learning augmented molecular dynamics framework “Reweighted Autoencoded Variational Bayes for enhanced sampling (RAVE)”. We study the two molecular systems, urea and glycine in explicit all-atom water, due to their enrichment in polymorphic structures and common utility in commercial applications. From our simulations, we observe back-and-forth liquid-solid transitions of different polymorphs, correctly ranking polymorph stabilities as $A > I > B$ -urea and $\gamma > \beta \geq \alpha$ -glycine. Finally, the machine learning based reaction coordinates allow for an in-depth analysis of the nucleation mechanism for both molecules, providing clear evidence of nonclassical two-step nucleation for both urea and glycine nucleation in water.

Molecular Simulations | Nucleation | Enhanced Sampling | Machine Learning

Introduction

Although traditionally viewed through the lens of classical nucleation theory (CNT) (1), which postulates the only important variable for describing nucleation and subsequent crystal growth is the size of the nascent crystal (2), more recent studies of nucleation for a number of physical systems under a variety of conditions via high-resolution experiments (3–5) and molecular dynamics (MD) simulations (2, 6–17) have shown that CNT alone is not sufficient for an accurate description of the mechanism of crystal formation, which often involves multiple, competing pathways (3, 18, 19). Thus it is of interest to discover other important variables besides or in addition to the size of the nucleus to accurately describe the nucleation process. One can imagine this situation is especially relevant for substances such as NaCl or organic molecules possessing multiple stable, crystalline structures or polymorphs, where both the lattice structure as well as crystal size are important in distinguishing the solid and the liquid states from each other.

From an experimental perspective, nucleation is a ubiquitous phenomenon, but the microscopic processes driving the nucleation event typically occur over time- and lengthscales that are, generally speaking, below the resolution of current physical apparatuses (3, 4). Thus, applying a combination of theory and simulation to describe the microscopic nature of nucleation is required to gain a detailed understanding of the molecular nature of the nucleation process and build a bridge

to the time- and lengthscales accessible by computational and experimental approaches.

Even with supercomputers capable of simulating hundreds of microseconds per day (20), the timescale for sampling most nucleation processes, occurring on the timescale of seconds, still remains out-of-reach. Since nucleation is a rare event from the microscopic perspective, nucleation events can generally only be observed in unbiased simulations under conditions of heavy supersaturation or by applying an external driving force. Thus, finding excellent reaction coordinates (RCs) along which the system can be biased to accelerate the sampling is still very much of importance through a variety of enhanced sampling methods (21–26). In parallel to the development of more powerful machines and sampling algorithms, there has also been an explosion in the use of machine learning (ML) techniques to sift and interpret the results of long simulations (27–32). Neural networks and ML in general have been implemented to discover good RCs for describing nucleation in a more automatic manner. These neural network derived RCs can then be used as the biasing coordinates in different enhanced sampling methods. In fact, even traditionally RC-free methods, such as path sampling methods (e.g. forward flux sampling) have been shown to benefit from a judicious choice of low-dimensional projections along which to calculate the flux (33, 34).

In principle, the RC can be directly expressed as a function of simple variables such as high-dimensional atomic po-

Significance Statement

Although a common occurrence experimentally, in many instances, a detailed picture of crystal nucleation remains unresolved. Computer simulations are helpful for gaining molecular insights regarding nucleation, but they tend to be limited by accessible timescales. To overcome these timescale limitations, we use a machine learning augmented molecular dynamics approach that automatically learns and biases along optimized reaction coordinates to enhance sampling of nucleation. We apply this procedure to aqueous solutions of urea and glycine, sampling multiple polymorphs for both and estimating their relative free energies. Our reaction coordinates give clear evidence of the presence of nonclassical two-step pathways for both systems. The protocol here should be generally applicable for all-atom resolution studies of nucleation in different environments.

ZZ, EB, ST, PT designed research. ZZ, EB performed research. ZZ, EB, PT wrote the manuscript.

There are no competing interests to declare.

[†] Ziyue Zou contributed equally to this work with Eric R. Beyerle.

¹ To whom correspondence should be addressed. E-mail: ptiwary@umd.edu

sitions. But, for various computational reasons, generally the RC is expressed as a linear or non-linear function of a lower-dimensional order parameters (OPs), which are able to distinguish metastable states. These OPs themselves are generally *a priori* designed functions of the atomic positions. Approximating the true RC with smoothly differentiable functions of the OPs has become one of the main aspects in study of crystal nucleation using enhanced sampling approaches such as well-tempered metadynamics (WTmetaD) (35), which is our interest in this work, but also more generally for other sampling approaches (12, 13, 36–51).

In this manuscript, we utilize a neural network framework termed the state predictive information bottleneck (SPIB) (52, 53) to extract a two-dimensional RC for describing the nucleation of different polymorphs of urea and glycine from solution. SPIB is a variant of RAVE that discovers a set of low-dimensional RCs capable of faithfully predicting the metastable states given the input OPs, which can then be biased in enhanced sampling simulations (53). The input OPs originate from a library of candidate OPs and are system specific (52, 53). For the nucleation processes studied here, the OPs are derived from a set reporting on the global and local orientations and packing of the nucleating species, e.g. coordination numbers (13, 54), radial distribution functions (55, 56), Steinhardt bond OPs (57), etc. We describe SPIB in more detail in [State Predictive Information Bottleneck](#).

We find that biasing MD simulations of urea and glycine in water using the RCs discovered by SPIB allows for a sufficient enhancement of the sampling such that multiple back-and-forth liquid to crystal polymorph transitions are observed over practical compute times on high-performance resources. Furthermore, through the use of a linear architecture during the encoding of the RCs, we are able to directly interpret the RCs discovered. Finally, by reweighting these biased simulations (58) the relative stability among crystalline phases sampled is ranked for both urea and glycine, which is found to be in excellent agreement with stabilities determined experimentally.

Discovering and Biasing Reaction Coordinates for Nucleation

Order parameters for nucleation. As mentioned in the Introduction, in this work as well as in work by others (12, 13, 36–49), it is common to build the reaction coordinate as a function of OPs that can collectively distinguish different competing metastable states. This has led to the development of several rich OPs for the study of nucleation and phase transitions in general, which we tabulate here.

1. *Coordination numbers and associated moments:* As introduced above, CNT is based on the size of the nucleus, and the formation of such crystal nuclei is closely related to the formation of a denser phase. A continuous and differentiable coordination number of any molecule i can be defined as:

$$c(i) = \sum_j \frac{1 - (r_{ij}/r_c)^6}{1 - (r_{ij}/r_c)^{12}} \quad [1]$$

where r_c is a radial cutoff and r_{ij} denotes the distance between reference sites for two molecules i and j . When averaged over all molecules in the system, the coordination

number can serve as an approximation to the true reaction coordinate in the study of gas-liquid transitions (13, 59, 60).

Inspired by this definition, in this manuscript we specifically consider two sets of populations of molecules, with coordination numbers greater than 8 and 11, denoted as N_{8+} , N_{11+} respectively. We also consider the second moment of all coordination numbers as an OP, denoted μ_c^2 (13, 54, 59). However, such coordination number based descriptors are not sufficient to describe the reaction coordinate in events like nucleation from the melt and polymorphism in molecular systems. This is because nucleation is accompanied with the appearance of a space group. Therefore, in addition to the OPs N_{8+} , N_{11+} and μ_c^2 derived from coordination number, we include other OPs into the dictionary of OPs, as introduced next.

2. *Steinhardt bond OPs:* These OPs, originally introduced in Ref. 57, have been used to distinguish Lennard-Jones solids (61–67) and extended to the study of ice polymorphs (68–72). They map a given local environment onto specific degrees of spherical harmonics (57), defined through :

$$q_{lm}(i) = \frac{\sum_j \sigma(r_{ij}) \mathbf{Y}_{lm}(\mathbf{r}_{ij})}{\sum_j \sigma(r_{ij})} \quad [2]$$

where \mathbf{Y}_{lm} is the l^{th} order of spherical harmonics and m ranges from $-l$ to l . As these bond OPs refer to distributions as superpositions of perfect crystalline structure, reliable results have been acquired in classifying face-centered-cubic (fcc), body-centered-cubic (bcc), hexagonal-close-packed (hcp) and liquid-like structures (61). Here, we add \bar{q}_4 , \bar{q}_6 from Ref. 57 corresponding to the average values of the fourth and sixth orders of spherical harmonics to our OP library. However, as pointed out by Dellago and Lechner (73) thermal fluctuations may destroy the ability in phase identification and as such the variants of original bond OPs have been developed for better differentiating ability at the expense of a higher computational cost which are omitted here.

3. *Interfacial water:* The contribution of solvent molecules can hardly be neglected when studying the nucleation of solvated systems (14). Here we introduce a new OP measuring approximately the population of interfacial waters or more generally solvent molecules surrounding solid-like solute molecules by using tunable distance cutoffs. This variable is defined as

$$N_s = \sum_i \frac{1}{2} \xi(i) c_{solvent}(i) \quad [3]$$

where

$$\xi(i) = \tanh(c_{solute}(i) - c_o) + 1 \quad [4]$$

Here i denotes a sum over solute molecules and c_o is a tunable parameter for the determination of solid-like aggregates which is set to be 5.0 for all systems in this work (54). Effectively, the OP in Eq. 3 is a product of two smoothed Heaviside functions: $\xi(i)$ only counts solute clusters larger than the threshold c_o , and $c_{solvent}(i)$ is a

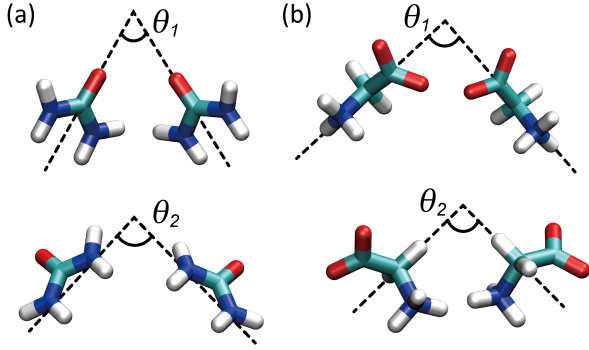


Fig. 1. Visualization of the feature vectors and corresponding intermolecular angles θ_1 and θ_2 for (a) urea and (b) glycine molecules. The feature vectors shown here are the vectors connecting C-O and N-N for urea, and C-N and C α -H α for glycine. Different atom types are indicated with different colors, specifically carbons in cyan, oxygens in red, nitrogens in blue, and hydrogens in white. Snapshots are rendered using Visual Molecular Dynamics (VMD) (75).

coordination number between such selected solute atoms and the solvent, as given in Eq. 1. Thus, N_s is large when two conditions are simultaneously satisfied: when the solute cluster is sufficiently large and also well-coordinated with solvent. If either one of these conditions is not satisfied, N_s is small. Thus, large values of N_s indicate cluster formation and low values indicate a liquid state or the presence of small, solvent-separated clusters.

4. *Averaged intermolecular angles:* The estimation of the size of solid-like aggregates and their solvation states is useful and intuitive for the study of molecular systems in different environments (13, 59, 60), but nucleation mechanisms can easily consist of non-classical behavior and polymorphs such that solely distance based OPs fail in categorizing them. In the spirit of Steinhardt bond OPs (57) and environment similarity OPs (74), we introduce a set of OPs which account for the orientation of molecular feature vectors of solutes to help better discriminate polymorphs. For any molecule i , we define:

$$\theta(i) = \frac{\sum_j \sigma(r_{ij})^{\frac{1}{2}} [(\pi - 2\tilde{\theta}) \tanh(5\tilde{\theta} - 9.25) + \pi]}{\sum_j \sigma(r_{ij})} \quad [5]$$

where $\tilde{\theta}$ is the angle formed between characteristic vector on molecule i and molecule j as illustrated in Fig. 1, and σ is a switching function of intermolecular distance. The hyperbolic tangent switching function is applied to remove the mirror image symmetry (see SI for detailed explanation). We then compute the mean of angular distribution functions, denoted as $\bar{\theta}_1$ and $\bar{\theta}_2$ where 1 and 2 denote the two intramolecular vectors specified for crystalline configuration identification (see Fig. 1 (a) and (b) for definitions of selected vectors for urea and glycine molecules, respectively). In addition to these OPs, we also consider in our OP dictionary the second moments $\mu_{\theta_1}^2$ and $\mu_{\theta_2}^2$ of the collection of θ values defined through Eq. 5.

5. *Pair entropy:* In Ref. 55 Piaggi and co-workers introduced an OP which approximates radial and orientational entropies from radial different distribution functions. This OP is formulated as:

$$S(r) = -2\pi\rho k_B \int_0^\infty [g(r) \ln g(r) - g(r) + 1] r^2 dr \quad [6]$$

where $g(r)$ is the radial distribution function, ρ is the density, and k_B is Boltzmann’s constant. This OP was introduced in order to account for the possible entropy-favored crystalline structures (56). An advanced version of this OP has been developed in Ref. 56. This pair orientational entropy OP denoted $S(r, \theta)$ depends on both the intermolecular distance and the relative angle θ between a given intramolecular vector equivalently defined for each solute molecule in the simulation:

$$S(r, \theta) = -\pi\rho k_B \int_0^\infty \int_0^\pi [g(r, \theta) \ln g(r, \theta) - g(r, \theta) + 1] \times r^2 \sin(\theta) dr d\theta \quad [7]$$

It was found (56) that such an approximation to the entropy is useful for distinguishing polymorphs in simulations of urea and naphthalene. Since Eq. 7 only accounts for a single angle, and not the three angles necessary to specify exactly the relative orientation between molecules, this expansion of the entropy, though useful, is necessarily approximate, as are the other OPs previously described in this section.

While individually these different OPs might have limitations, they can supplement each other and provide a palette through which the complex molecular processes governing nucleation can be described. It is by combining them through the State Predictive Information Bottleneck (SPIB) (52) approach that we construct low-dimensional projections that are much closer to the true RC than any of the OPs on their own. We next briefly summarize the SPIB approach, referring to Ref. 52 for further details.

State Predictive Information Bottleneck (SPIB). Given the evidence that CNT is insufficient to accurately describe the nucleation event for a number of chemical systems, for instance because knowledge of more than just the solute coordination number OP is required, we need an approach to combine the different possible OPs to develop a lower-dimensional reaction coordinate for describing nucleation in urea and glycine.

Here we utilize a machine learning method known as the state predictive information bottleneck (SPIB) (52, 53, 77), which takes the form of a variational autoencoder (VAE) (78, 79). SPIB differs from the traditional VAE because instead of attempting to maximize the model’s ability to re-construct the input from the low-dimensional latent space, it instead maximizes the quality of reproducing the population of the system’s metastable states after a given lagtime τ in the future. That is, the SPIB finds the latent space that best reproduces the metastable state populations at time $t + \tau$ given the values of the input OPs at time t (52). This approach allows SPIB to simultaneously perform dimensionality reduction and accurate

Table 1. Parameters for WTmetaD

System	ω (kJ/mol)	γ	σ_1 (RC unit)	σ_2 (RC unit)	T (K)
Urea	5.0	100	0.2	0.2	300
Glycine	5.0	100	1.15	1.15	300

future state prediction by minimizing a loss function that is inspired by the variational information bottleneck formalism (52, 80, 81).

Conceptually, this approach is similar to performing a Markov state model and clustering analysis (82, 83) with a continuous basis set. In SPIB the number and neighborhood of each metastable state is adjusted on-the-fly during the training of the model. The final learned model is output once the neighborhoods spanned by each metastable state have converged to below a pre-defined threshold that is a tunable hyperparameter of the model.

Finally, since biased simulations are input to the SPIB, normally the WTmetaD weights would be used in the analysis to account for the sampling from a biased distribution (53). For urea and glycine, we find that the barriers to nucleation from the liquid state are so large (~ 100 kJ/mol or more) that using the metadynamics weights in the analysis effectively destroys any polymorph minima on the surface, yielding a single, global minimum corresponding to the liquid state (more details in the SI). Since SPIB finds the RC describing transitions between metastable minima, the metadynamics weights must be neglected in this case to find an effective set of RCs for nucleation.

Estimating free energies with Metadynamics. In order to learn the SPIB, or the approximate RC, as a combination of different OPs, we need access to a trajectory that has visited different possible conformations. Such a trajectory is generated here through the method Metadynamics, which helps the system escape free energy minima by periodically depositing Gaussian kernels as a function of the variable being biased. For the initial metadynamics runs we bias orientationally informative OPs such as intermolecular angles $\bar{\theta}$ and orientational entropies S_{θ} . After performing SPIB analysis on these runs, we then bias along the SPIB-learned RCs in future iterations. In particular, here the well-tempered variant of metadynamics (WTmetaD) is used where kernels are decreased in height for biasing regions

being revisited, thus leading to better convergence of the free energy surface (35). The WTmetaD parameters are reported in Table 1. The height of Gaussian deposition, ω , is selected to $2 k_B T$ at 300 K and the bias factor, γ , is set to be 100, in order to overcome high energy barrier associated with nucleation problems (84). The width of the Gaussian, σ , is set to the thermal fluctuation of corresponding approximate reaction coordinate estimated from a short (~ 10 ns) unbiased MD run.

After classifying frames in the biased simulation into either the liquid state or a particular crystal polymorph, the free energy difference between two states a and b at temperature T can be calculated as follows:

$$\Delta G_{a \rightarrow b} = G_b - G_a = k_B T \log \frac{P_a}{P_b} \quad [8]$$

where k_B is Boltzmann’s constant and P_a , P_b denote the Boltzmann probabilities of states a , b obtained from reweighting the WTmetaD simulations (58).

Results and Discussion

We performed classical all-atom MD simulations for all systems using GROMACS version-2022.2 (85) patched with PLUMED 2.6.1 (86, 87) to perform the WTmetaD. Further simulation details are provided in Methods. Below we provide detailed results first for Urea followed by Glycine.

Urea.

Urea Nucleation. Urea is commonly used as fertilizer and as an ingredient for nitrogen resources for organic synthesis. Due to this industrial importance, urea has been studied extensively and several crystalline structures have been synthesized and reported. These include polymorphs named I (space group: $P4_21m$), III ($P2_12_12_1$), IV ($P2_12_12$) and V ($Pmcn$), where polymorph I corresponds to the typical isoform stabilized at ambient conditions and the rest are high-pressure, high-temperature products (88–94). Moreover, an ever-enriched

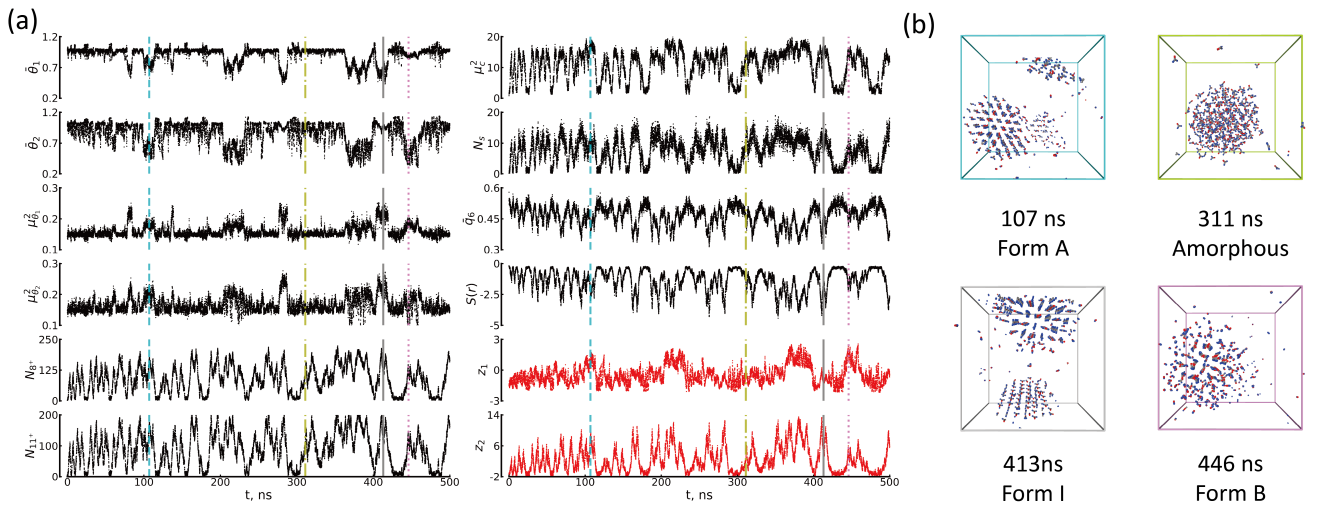


Fig. 2. Sampling different urea polymorphs with WTmetaD simulations biasing the SPIB-learned 2-dimensional reaction coordinate. (a) shows a representative time series of OPs (black) and reaction coordinates (red), clearly demonstrating multiple back-and-forth transitions between different phases. Vertical cyan dashed, green dash-dotted, grey solid, and pink dotted lines indicate representative transitions to form A, amorphous, form I, and form B from initial liquid phase. (b) shows snapshots of structures sampled during trajectory shown in (a), along with the time (vertical lines in (a)) at which they were observed. Ovito 3.3.5 (76) was the visualization tool used for snapshot generation.

dictionary of polymorphism in urea has been established with computational methods with classical and quantum approaches (14, 56, 84, 95–98). We adopted the same notations as in Ref. 56, where two more polymorphs of urea A ($Pnma$) and B($P\bar{1}$) were introduced. It remains unknown if these two crystal structures A and B are artifacts due to GAFF (99) force field or simply experimentally yet to be observed. Despite the orientational difference in the lattice cell, hydrogen bonding pattern in both forms A and B (all in type III) has been shown to be different from experimental forms (type I and type II) (97, 98).

Chronologically, we start with a preliminary round of well-tempered metadynamics to facilitate state-to-state transitions along trial reaction coordinates. For this, we biased the two averages of the two feature angles (Fig. 1 (a)), $\bar{\theta}_1$ and $\bar{\theta}_2$ as they had been considered as OPs in distinguishing crystal structures of urea from each other (44). Several transitions to and from the solid states of interest are observed in the WTmetaD simulations (data not shown) biasing this two-dimensional coordinate (4 independent runs of 400 ns each, totalling 1.5 ms) and trained as input data for SPIB along with other candidate OPs.

Urea Polymorphism. From this preliminary WTmetaD simulation, we performed SPIB to learn a 2-d latent representation for the reaction coordinate (denoted as z_1 and z_2) as linear combinations of OPs discussed in **Materials and Methods**. We then perform a second round of WTmetaD biasing along this SPIB learned 2-d RC consisting of 4 independent runs of 500 ns each. The time series for different OPs and the 2-d RC components are shown in Fig. 2(a) in black and red respectively. This unequivocally shows the presence of numerous back and forth state-to-state transitions, a hallmark of good enhanced sampling (100). In particular, three crystal structures, namely polymorphs I, A, and B, are visited during simulations. The corresponding snapshots for these from one are shown in Fig. 2(b) along with that of an amorphous bulk phase. The evidence for the formation of these polymorphs can be found in the time series of intermolecular angle OPs (top left two rows in Fig. 2(a)), as either one or both of these OPs drop, indicating formation of an ordered phase based on their definitions.

In Fig. 3(a), the reweighted free energy surface along the two-dimensional latent representation z_1 and z_2 is plotted (58). The states of interest, one liquid and three solid phases, have been labeled on this surface. In Fig. 3(b), we provide the coefficients for different OPs, indicating how much they contribute to the RC (see Methods for details on calculating these coefficients). From these bar plots, it can be seen that several OPs are weighted heavily in the RC, comprising attributes of intermolecular angle and coordination number. Referring to the definition of these two categories of OPs, the coordination number is a simple but useful OP in the identification of phases, suggestive of the CNT formalism where only size of the nucleating cluster is sufficient. However Fig. 3(b) clearly shows that the coordination number in such complicated molecular systems is not enough for capturing the slow degrees of freedom for crystallization. In addition, our RC indicates that the orientation of feature vectors needs to be taken into account. One possible explanation for this would be that the coordination number part of the RC collects molecules of interest together to form clusters or a pre-nucleus, and possibly sub-

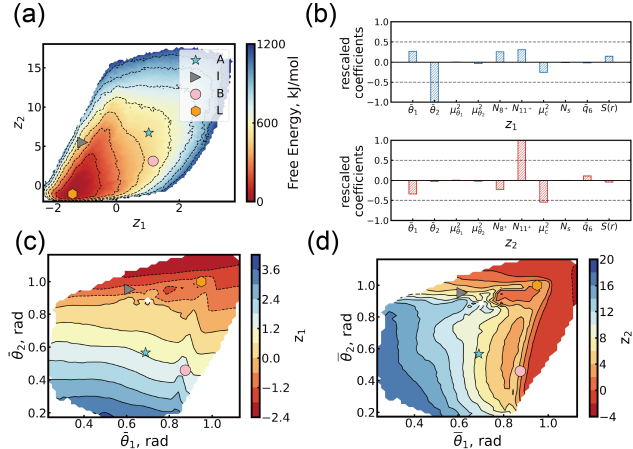


Fig. 3. (a) Reweighted free energy surface in kJ/mol along SPIB-learned reaction coordinates with landmarks for states of interest (solid states A, I, B, and liquid state L). (b) Rescaled coefficients for each OP in construction of SPIB-learned RCs. The coefficients are rescaled with respect to the corresponding fluctuations of components in WTmetaD simulations (see **Materials and Methods** for details). The importance of urea molecules relative orientation can be seen from the first reaction coordinate while the second coordinate shows the relevance of clustering. (c) z_1 -projection onto $(\bar{\theta}_1, \bar{\theta}_2)$ space; and d) z_2 -projection onto $(\bar{\theta}_1, \bar{\theta}_2)$ space. The markers asterisks (cyan), triangles (grey), circles (pink) and hexagons (orange) indicate crystalline structures A, I, B and liquid phase L, respectively.

sequent to this step, the angular part of the RC helps order this pre-nucleus into different crystalline structures. This is indeed similar to the nonclassical two-step nucleation mechanism which has been widely observed in both experiments and simulations (18, 101–105).

To support the above rationale, we project the SPIB-learned RCs z_1 and z_2 used to bias onto orientational informative OP space $(\bar{\theta}_1, \bar{\theta}_2)$ in Fig. 3(c) and (d) respectively. Here it can be seen that the driving forces behind the two representations are clearly different. z_1 specifically enforces the transitions from initial liquid state (orange hexagon) to states with lower $\bar{\theta}_2$ values (which are form A (cyan star) and form B (pink circle)) and it shows strong correlation to $\bar{\theta}_2$ OP itself. On the other hand, z_2 pushes the system away from liquid state to all potential solid phases.

Comparison with previous studies. For the purpose of accurate classification of crystal structures for further analyses, the local crystallinity (SMAC) OPs are used (see SI for full expressions) (14, 84, 95, 106). In this way, polymorphs can be screened precisely by properly positioning the centers of various switching functions. The size of the nucleus can then be computed using graph theoretic algorithms (107). After this classification, the free energy corresponding to each phase can be evaluated, giving the free energy difference between two arbitrary states a and b at temperature T as described in **Estimating free energies with Metadynamics**. Fig. 4 shows the free energy differences of different forms of solid urea with respect to the initial liquid phase obtained after reweighting the biased WTmetaD simulations (58). As can be seen from this figure, our simulations suggest that form A is the most stable polymorph, followed by form I and finally form B. The relative stability of forms A and I is in agreement with previous computations from Ref. 84 using the same force-

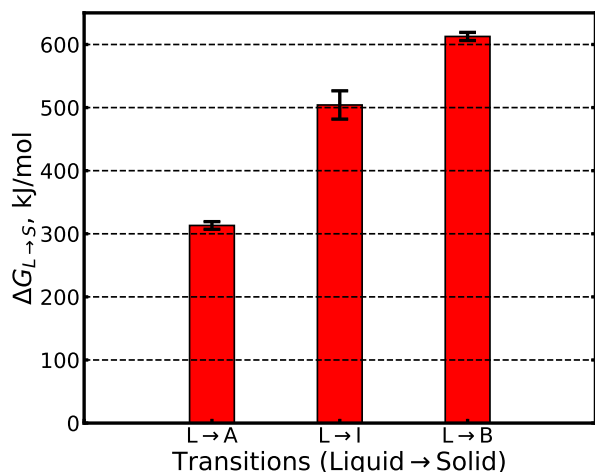


Fig. 4. Free energy difference in kJ/mol between different polymorphs with respect to liquid state as calculated from WTmetaD simulations. This indicates that form A is more stable than form I and form B is the least stable among the three solid phases, comparatively. The error bar is computed over four independent product runs.

fields as this work. However, to the best of our knowledge, metastable state B has never been synthesized in aqueous solution of urea, and its very high free energy relative to the other forms may explain why such a structure is difficult to sample. We can rationalize why we were able to sample this metastable polymorph in our simulations and also in Ref. 56. Structurally, form B has a completely different orientation among other polymorphs in which its dipole moment in the direction of C-O vector is no longer parallel or anti-parallel to its neighbors. This is likely a result of entropic contributions (56). By having entropy-related OPs in our dictionary of OPs that comprise the RC, we are able to accelerate the substantial entropic degrees of freedom together with other more energy dominated modes, and therefore both enthalpic and entropic-favored crystalline structures of urea are formed.

Glycine.

Glycine Nucleation. Glycine is the simplest amino acid, with its R-group consisting of a single hydrogen atom (108). Glycine has multiple physiological functions: it serves as a precursor to more complex biomolecules such as heme, purines, creatine, and more complex amino acids; glycine is also an inhibitory neurotransmitter (109) and is involved in cytoprotection and immune system function (110). Glycine forms three well-known polymorphs from solution called the α (space group: $P2_1/n$), β ($P2_1$), and γ ($P3_1$) polymorphs; thermodynamically, γ -glycine is the most stable, but α -glycine tends to be the form that crystallizes from solution at neutral pH and ambient atmospheric pressure (111–114). Several other high-pressure polymorphs have been discovered (114, 115), but they are not typically observed at atmospheric pressures or temperatures. For performing the WTmetaD (35) simulations of glycine, we use a similar OP library as urea, with one major exception: the pair entropy $S(r)$ is swapped for the orientational pair entropy $S(r, \theta)$ (56). The angles used for calculating $S(r, \theta)$ are those given in Fig. 1(b). For glycine, the first intramolecular vector is defined as that from the N-terminal nitrogen to the C-terminal carbon atom; the second intramolecular vector starts at the alpha-carbon C_α , and ends at the R-group hydrogen

atom H_α .

In contrast to urea, we find it necessary to include $S(r, \theta)$ in the OP library because, without it, reversible nucleation events are not observed (data not shown). We postulate that this increased importance in the case of glycine is due simply to $S(r, \theta)$ being a two-body term and, hence, a first-order order correction to the excess entropy of a fluid (116, 117) compared to the entropy of an equivalent ideal gas. Since glycine is more massive and zwitterionic, as well as possessing a stronger dipole moment, it is less ideal in the liquid phase compared to urea and, therefore, it is to be expected that it will possess more excess entropy compared to urea, making it necessary to place $S(r, \theta)$ and not just $S(r)$ in the OP library.

For the preliminary round of WTmetaD, we bias along $S(r, \theta_1)$ and $S(r, \theta_2)$ since these OPs were found to give the best sampling from the OP library. This 400ns preliminary simulation is described in detail in the SI. As with urea, the trajectories of the OPs from this preliminary simulation are used as input data for training SPIB.

Glycine Polymorphism. Here we are interested in the α -, β -, and γ -glycine polymorphs observed at ambient temperature and pressure (114). A necessary but not sufficient method (118) to differentiate the three polymorphs is through the collective orientation of the C-N vectors (Fig. 1(b)). For α -glycine, C-N vectors alternative in layers of two in a ‘positive’ orientation (C-N) followed by a ‘negative’ orientation (N-C) repeating. For β -glycine, positive and negative layers alternate one at a time. In γ -glycine, all layers of the crystal possess the same orientation, either all positive or all negative. Using only the C-N axis orientations to classify polymorphs, we find a relative stability rank order of form- γ > form- β \geq form- α , which recovers form- γ as the most stable form in agreement with experiments of bulk glycine (112, 114).

While this classification approach correctly accounts for the large-scale orientation of the crystal, it ignores the local orientation, such as hydrogen bond patterns and relative angles and distances between layers of the crystal (114, 119). This coarse procedure for identifying polymorphs is selected over the more rigorous one given in Ref. 120, which has not been tested for use in nucleation from solution or long timescale simulations, where there can be significant perturbations to the crystal structure. Based on these considerations, we have chosen to characterize the polymorphs using the relative orientation of monomers along the axis parallel to the C-N vector only. Ignoring local structure, this protocol will introduce some contamination of the polymorph classification. Furthermore, the crystal structures of glycine are much more similar to each other compared to urea, making the SMAC protocol used for urea ineffective for glycine (details in the SI). Since this study is, to our knowledge, the first to perform enhanced sampling simulations of glycine to study nucleation without seeding in water alone at or below the saturation concentration, our reported numbers at the very least have qualitative significance in being able to correctly rank order glycine polymorph stability in pure aqueous solution.

Fig. 5 shows α -glycine, β -glycine and γ -glycine in Figs. 5(a–c) respectively. From all three snapshots, the appropriate orientations for each polymorph along the monomer C-N axis should be apparent, although, given the size of the system (72 glycine molecules), finite volume and surface area effects are likely to be significant due to the large surface area to

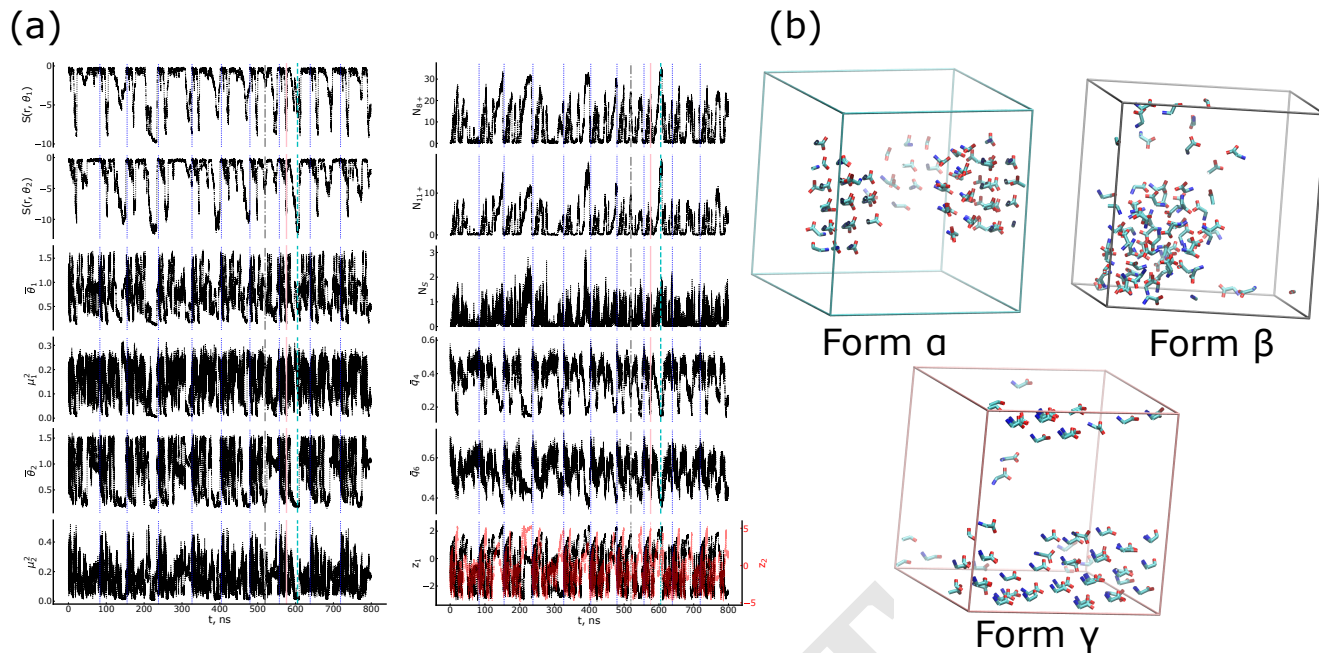


Fig. 5. Sampling glycine polymorphs with WTmetaD simulations biasing the SPIB-learned 2-dimensional reaction coordinate. (a) shows the time series of the OPs (black) and SPIB RCs (black, z_1 ; red, z_2) from the ten replicate simulations of glycine, with each trajectory demarcated by the dotted blue lines. Vertical cyan dashed, gray dashed-dot, and pink solid lines indicate representative transitions to form α , form β , and form γ from the liquid phase. (b) shows snapshots of the polymorph structures sampled during trajectories shown in (a); color of the box framing each snapshot corresponds to the color of the vertical time slice in (a). Hydrogen atoms on glycine and water molecules are removed for clarity; snapshots are rendered using VMD.

volume ratio of the clusters. We also expect solvent-induced perturbations compared to the respective crystal structures (121, 122) from the melt.

An analysis of the SPIB RCs used to bias the nucleation simulation of glycine is given in Fig. 6. In Fig. 6(a), the reweighted free energy surface along the 2-d linear SPIB latent space used as the biasing variables in metadynamics is shown with the locations of the putative α -, β -, and γ -glycine polymorphs labeled with colored stars; for reference, the liquid (isotropic) state is also labeled with a magenta star. Fig. 6(a) shows that, while none of the glycine polymorphs are located in free energy minima they are neither at free energy maxima, which indicates that the SPIB RCs are doing a reasonable job sampling the crystal polymorphs.

Fig. 6(b) shows the rescaled contribution of each input variable to the final two-dimensional SPIB model. For both RCs, the orientational entropies are weighted heavily in-line with the physical intuition explained in [Glycine nucleation](#) that higher-order corrections to the entropy of the zwitterionic glycine will be more important than an uncharged molecule such as urea. Also highly weighted are the two angular coordinates, $\bar{\theta}_1$ and $\bar{\theta}_2$, which justifies performing the polymorph labeling and analysis in that subspace.

The SPIB RCs are further interpreted by projecting them onto the $(\bar{\theta}_1, \bar{\theta}_2)$ subspace in Figs. 6(c), (d). The first SPIB RC, z_1 , corresponds to nucleation from the liquid to the three common polymorphs labeled on the surface. Examining the contours more closely, it specifically describes transformation from the liquid and γ -glycine states, which are the two most populated states observed in our simulations, to the α - and β -glycine polymorphs. There is also a strong correlation of $\bar{\theta}_1$ with z_1 , as expected from Fig. 6(b). The second SPIB RC, z_2 ,

corresponds to transitions from the liquid state to γ -glycine via the α and β polymorphs. Interestingly, this mechanism of transition from the liquid state to the most stable crystal polymorph (form γ) via the less stable crystal polymorphs (forms α and β , Figure 7) is consistent with the Ostwald step rule (123) and is evidence for two-step nucleation in aqueous glycine, which already has been observed experimentally (124). This RC also correlates strongly with transitions from low-to-high values of $S(r, \theta_1)$ (data shown in the SI), again as expected from Fig. 6(b).

In summary, we find the linear RCs discovered by SPIB are able to 1) separate the common glycine polymorphs in the two-dimensional RC space and 2) yield a reasonable and interpretable set of reaction coordinates for describing nucleation of glycine from aqueous solution.

Comparison with experimental measurements. To our knowledge, no free energy differences between polymorphs for crystallization from aqueous solution for glycine has been reported in the literature. Solubility experiments in pure water have been reported in Ref. 125, where the authors find that in water, the α polymorph is the most soluble, followed by the γ polymorph, then the β polymorph, which is completely insoluble in pure water (125). Thus, this solubility series implies that in aqueous solution the β polymorph should have the lowest free energy barrier to crystallization in aqueous solution since it is completely insoluble in water, followed by γ -glycine, then α -glycine with the highest barrier to crystallization. Thus, the barrier to crystallization should be the inversely related to the polymorph’s solubility in water. This relative stability is also consistent with that given for glycine in melt (112), where those authors find order of stability given as form- γ > form-

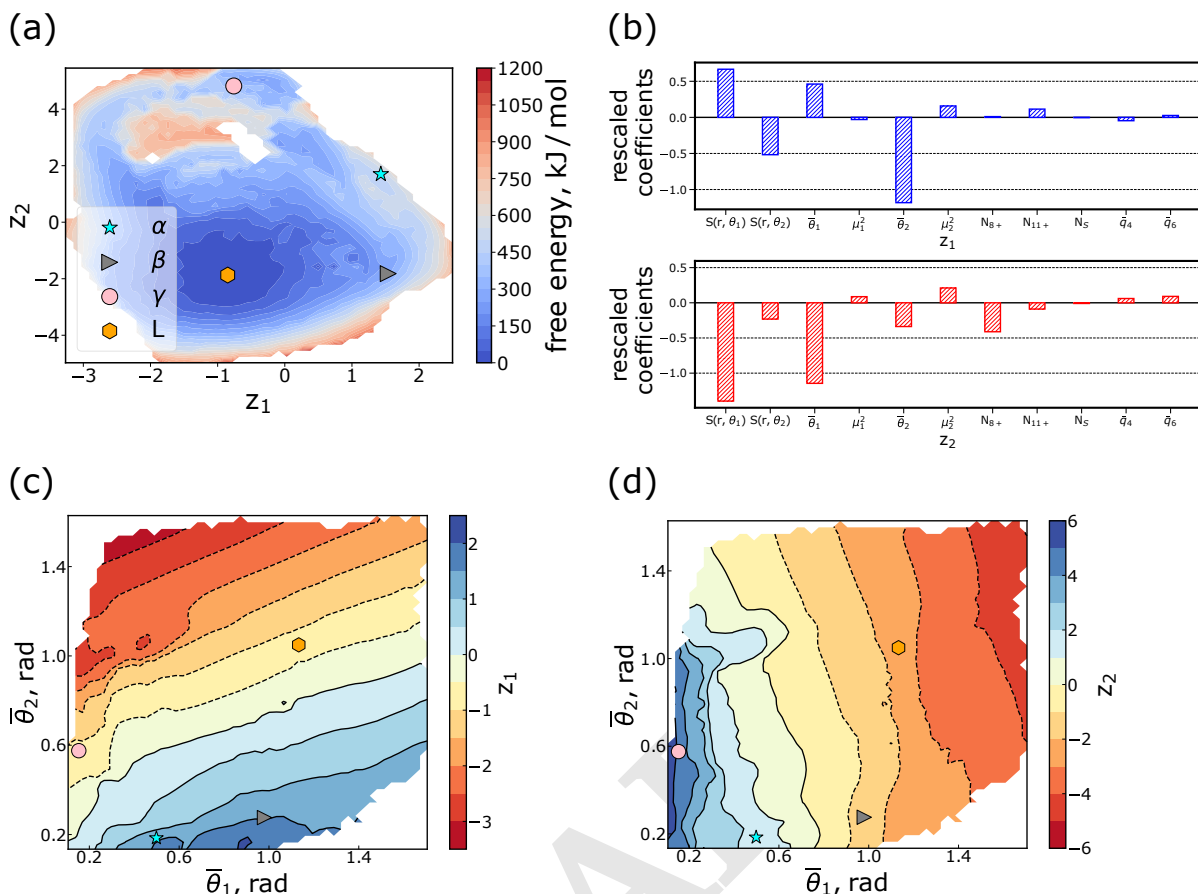


Fig. 6. (a) Reweighted free energy surface in kJ/mol in the two-dimensional space of the linear SPIB RCs, which were used as the metadynamics biasing variables. Markers show the locations of the putative glycine polymorphs sampled during the simulation: liquid, orange hexagon; α , cyan star; β , grey sideways triangle; and γ , pink circle. (b) SPIB coefficients from the linear model, reweighted by the standard deviation of the input variable. For the first SPIB RC (top panel, blue bars), the most important input variables is the trajectory of the average second intermolecular angle $\bar{\theta}_2$, and the orientational entropy $S(r, \theta_1)$. For the second SPIB RC (bottom panel, red bars), the two most important input variables are $\bar{\theta}_1$ and its orientational entropy $S(r, \theta_1)$. (c) The first SPIB RC z_1 projected into the $(\bar{\theta}_1, \bar{\theta}_2)$ subspace. Colored stars show the locations of the putative glycine polymorphs, with the coloring identical to that in panel (a). (d) is the same as (c), except the projection is of the second SPIB RC, z_2 .

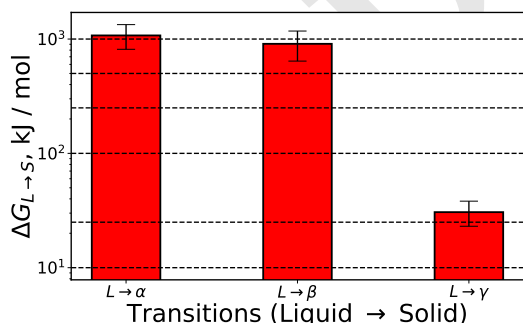


Fig. 7. Free energy difference in kJ/mol between different polymorphs with respect to liquid state as calculated from WTmetaD simulations. This result indicates that form γ is more stable than form β , which is slightly (though not significantly) more stable than form α . Error bars are one standard error of the mean over the ten replicate simulations.

$\alpha > \text{form-}\beta$, while in this work we find $\text{form-}\gamma > \text{form-}\beta \geq \text{form-}\alpha$ (Figure 7).

This relative stability ranking disagrees with the seeded cluster MD simulations reported in Ref. 126, where the authors find that β -glycine is more stable than α -glycine, which is more

stable than γ -glycine. Their experiment and analysis differ from ours in that 1) the authors of Ref. 126 use pre-seeded molecular dynamics simulations of glycine with much larger ($> 1 \times 10^3$ glycine molecules) simulations and 2) the free energy differences are computed using CNT, whereas we are calculating the free energy difference using the reweighted state probabilities calculated directly from the biased simulation statistics along an optimized RC as opposed to the simplistic RC in CNT. Our analysis of glycine clusters significantly smaller than the CNT-predicted critical cluster size (~ 300 glycine molecules, using the parameters from Ref. 126) could be another major reason for the differences in reported polymorph stability.

Conclusion

Although nucleation is a frequent event on the experimental and biological timescales, with currently accessible compute resources nucleation is a rare event computationally, even when utilizing enhanced sampling techniques (11, 13, 36, 44, 59, 95, 127). Thus, even for relatively simple systems such as aqueous urea and glycine systems studied here, sampling polymorph configurations and, more dauntingly, determining relative thermodynamic stabilities of these

polymorphs, is difficult computationally. In this work we have demonstrated a more-or-less automatable protocol to obtain back-and-forth sampling of different polymorphs in aqueous solution. Specifically, we have shown here that good sampling of polymorphs is possible when classical molecular dynamics simulations of urea and glycine are biased along optimized reaction coordinates found using the machine learning approach State Predictive Information Bottleneck (SPIB) (52) which belongs to the RAVE family of methods (27, 128). A linear, two-dimensional approximation to the reaction coordinate extracted from SPIB (52) can be used to 1) effectively bias nucleation simulations of aqueous urea and glycine to enhance the sampling of polymorph nucleation, and 2) interpret the SPIB RCs to determine which OPs are the most important drivers of nucleation.

When interpreting the RCs derived from the SPIB analysis, we find that for urea, the intermolecular angle and cluster size OPs are the most important contributors to the RC; for glycine, the intermolecular angles and orientational entropy of these angles are the most important to determining the reaction coordinate. These observations reflect that size informative OPs suggested by CNT are insufficient in describing slow modes towards nucleation of urea and glycine molecules; in addition orientational OPs are also needed. Each polymorph is identified using different metrics and then ranked appropriately as per their Boltzmann weights at 300 K (58). The relative stability found by us shows form-A > form-I > form-B for urea and form- γ > form- β \geq form- α for glycine. Both rankings show agreements to the literature besides structures yet experimentally observed. Since we performed the SPIB analysis on the unweighted energy surface, we cannot yet offer any kinetic insights regarding the nucleation of either organic molecule studied here. In addition we did not consider the question of finite size effects, which would especially impact kinetic properties. This will be done in future work using approaches such as Ref. 59. Secondly, our simulations would have been more representative of supersaturation levels of experiments with the use of constant chemical potential ensemble, which is an active area of research for studying nucleation (127).

To summarize, this work makes several significant contributions to the field of nucleation research and enhanced sampling in general. We have applied deep learning based RC construction methods to arguably the most complex set of systems to date and used them to successfully find reaction coordinates that accelerate the nucleation process of multiple polymorphs for both urea and glycine aqueous solutions. Furthermore, the simulations of glycine reported here are the first, to our knowledge, to utilize metadynamics to induce nucleation of the amino acid in water. Based on these results, we believe using machine learning methods to construct approximate reaction coordinates can provide novel solutions and information regarding non-classical effects in the nucleation of molecules from aqueous media.

Associated Content

Supporting Information. The Supporting Information is available free of charge at xxx. It contains detailed further numerical analyses for different systems.

Notes. The code needed to reproduce the models used in this work is available at github.com/tiwarylab. The input files necessary to reproduce the simulations done in this work will be available on PLUMED NEST at <https://www.plumed-nest.org/>.

Materials and Methods

Simulations setup. A $5.0\text{ nm} \times 5.0\text{ nm} \times 5.0\text{ nm}$ simulation box containing 300 urea and around 3300 TIP3P (129) water molecules is built to mimic the work of Salvalaglio *et al* (84). The partial charges of urea were adopted from the Amber03 (130) database. For the aqueous simulations of glycine, we follow the simulation protocol established in Ref. 131. A simulation box of size $3.6\text{ nm} \times 3.6\text{ nm} \times 3.6\text{ nm}$ is constructed with 72 glycine molecules and ~ 1200 SPC/E (132) water molecules with generalized Amber force field (GAFF) (99), and the charges on glycine are those derived using the CNDO methodology in Ref. 133. This combination of the GAFF and CNDO charges for glycine is utilized because it has been found to accurately reproduce the physical properties of both aqueous and crystalline glycine as well as inducing α -glycine crystallization from solution (134). The glycine simulations correspond to a saturated glycine solution (whose molality is experimentally measured to be 3.33 mol/kg) (131). However, since the level of supersaturation is known to be one of the driving forces of nucleation in solvated system and solubilities measured with computational methods tend to be underestimated comparing to experiments due to finite size effect and force field limits (135), the system might be considered as supersaturated under the particular force field utilized here.

For both the systems, all MD and metadynamics simulations were performed in the constant number, pressure, temperature (NPT) ensemble with an integration time step of 2 fs. Systems were coupled with a thermostat of velocity rescaling scheme (136) at 300 K. The pressure was controlled using the Parrinello-Rahman barostat (137) at 1 bar. The relaxation times to thermostat and barostat were 0.1 ps and 1 ps, respectively, for both system investigated. Particle-mesh Ewald method (138) was used for the computation of long range electrostatic interaction and hydrogen bonds were constrained with the LINCS algorithm (139). The cutoffs of electrostatic and Van der Waals interaction in real space were selected to be 1.2 nm for glycine and 1.0 nm for urea.

Rescaling Coefficients of SPIB-learned Representations. As the coefficients learned by SPIB are in dimensions of the inverse of the corresponding OPs and unstandardized as input, proper rescaling of these coefficients is needed for the purpose of evaluating the importance of each OP to the RC. Following the “betasq” protocol from Ref. 140, these rescaled coefficients are calculated as the product of the coefficients learned by SPIB and the fluctuation of the OP individually from the input trajectories (WTmetaD simulations biasing $\bar{\theta}_1$ and $\bar{\theta}_2$ OPs).

Acknowledgments

The authors thank Dr. Pablo M. Piaggi for providing source codes for the entropy OPs. We also thank Prof. John D. Weeks, Prof. Matteo Salvalaglio, Dr. Yihang Wang, Dr. Ruiyu Wang, Zachary Smith, Luke Evans, Dedi Wang, and Renjie Zhao for discussions and Luke Evans for proofreading the manuscript. This research was entirely supported by the

U.S. Department of Energy, Office of Science, Basic Energy Sciences, CPIMS Program, under Award DE-SC0021009. We also thank Deepthought2, MARCC and XSEDE (141) (projects CHE180007P and CHE180027P) for computational resources used in this work.

- B Peters, *Reaction Rate Theory and Rare Events Simulations*. (Elsevier, Amsterdam), (2017).
- S Karthika, T Radhakrishnan, P Kalaichelvi, A review of classical and nonclassical nucleation theories. *Cryst. Growth & Des.* **16**, 6663–6681 (2016).
- MH Nielsen, S Aloni, JJ De Yoreo, In situ tem imaging of caco3 nucleation reveals coexistence of direct and indirect pathways. *Science* **345**, 1158–1162 (2014).
- T Nakamuro, M Sakakibara, H Nada, K Harano, E Nakamura, Capturing the moment of emergence of crystal nucleus from disorder. *J. Am. Chem. Soc.* **143**, 1763–1767 (2021) PMID: 33475359.
- JJD Yoreo, et al., Crystallization by particle attachment in synthetic, biogenic, and geologic environments. *Science* **349**, aaa6760 (2015).
- PM Piaggi, J Weis, AZ Panagiotopoulos, PG Debenedetti, R Car, Homogeneous ice nucleation in an ab initio machine-learning model of water. *Proc. Natl. Acad. Sci.* **119**, e2207294119 (2022).
- RA LaCour, TC Moore, SC Glotzer, Tuning stoichiometry to promote formation of binary colloidal superlattices. *Phys. Rev. Lett.* **128**, 188001 (2022).
- AA Bertolazzo, D Dhabal, V Molinero, Polymorph selection in zeolite synthesis occurs after nucleation. *The J. Phys. Chem. Lett.* **13**, 977–981 (2022) PMID: 35060725.
- LC Jacobson, W Hujo, V Molinero, Amorphous precursors in the nucleation of clathrate hydrates. *J. Am. Chem. Soc.* **132**, 11806–11811 (2010) PMID: 20669949.
- AG Shtukenberg, et al., Melt crystallization for paracetamol polymorphism. *Cryst. Growth & Des.* **19**, 4070–4080 (2019).
- F Giberti, GA Tribello, M Parrinello, Transient polymorphism in nacl. *J. chemical theory computation* **9**, 2526–2530 (2013).
- AR Finney, M Salvalaglio, Multiple pathways in nacl homogeneous crystal nucleation. *Faraday Discuss.* (2022).
- ST Tsai, Z Smith, P Tiwary, Reaction coordinates and rate constants for liquid droplet nucleation: Quantifying the interplay between driving force and memory. *The J. chemical physics* **151**, 154106 (2019).
- M Salvalaglio, T Vetter, F Giberti, M Mazzotti, M Parrinello, Uncovering molecular details of urea crystal growth in the presence of additives. *J. Am. Chem. Soc.* **134**, 17221–17233 (2012).
- H Niu, YI Yang, M Parrinello, Temperature dependence of homogeneous nucleation in ice. *Phys. Rev. Lett.* **122**, 245501 (2019).
- G Gobbo, MA Bellucci, GA Tribello, G Ciccotti, BL Trout, Nucleation of molecular crystals driven by relative information entropy. *J. Chem. Theory Comput.* **14**, 959–972 (2018) PMID: 29272581.
- B Abécassis, et al., Persistent nucleation and size dependent attachment kinetics produce monodisperse pbs nanocrystals. *Chem. Sci.* **13**, 4977–4983 (2022).
- J De Yoreo, More than one pathway. *Nat. Mater.* **12**, 284–285 (year?).
- J De Yoreo, *A Perspective on Multistep Pathways of Nucleation*. (ACS Publications), pp. 1–17 (2020).
- DE Shaw, et al., Anton 3: Twenty microseconds of molecular dynamics simulation before lunch in *Proceedings of the International Conference for High Performance Computing, Networking, Storage and Analysis*, SC '21. (Association for Computing Machinery, New York, NY, USA), (2021).
- G Torrie, J Valleau, Nonphysical sampling distributions in monte carlo free-energy estimation: Umbrella sampling. *J. Comput. Phys.* **23**, 187–199 (1977).
- A Laio, M Parrinello, Escaping free-energy minima. *Proc. Natl. Acad. Sci.* **99**, 12562–12566 (2002).
- RJ Allen, PB Warren, PR ten Wolde, Sampling rare switching events in biochemical networks. *Phys. Rev. Lett.* **94**, 018104 (2005).
- T Lazaridis, M Karplus, Orientational correlations and entropy in liquid water. *The J. Chem. Phys.* **105**, 4294–4316 (1996).
- P Rosales-Pelaez, I Sanchez-Burgos, C Valeriani, C Vega, E Sanz, Seeding approach to nucleation in the *nvt* ensemble: The case of bubble cavitation in overstretched lennard jones fluids. *Phys. Rev. E* **101**, 022611 (2020).
- VE Bazterra, MB Ferraro, JC Facelli, Modified genetic algorithm to model crystal structures. i. benzene, naphthalene and anthracene. *The J. Chem. Phys.* **116**, 5984–5991 (2002).
- Y Wang, JML Ribeiro, P Tiwary, Machine learning approaches for analyzing and enhancing molecular dynamics simulations. *Curr. Opin. Struct. Biol.* **61**, 139–145 (2020).
- M Ceriotti, Unsupervised machine learning in atomistic simulations, between predictions and understanding. *The J. chemical physics* **150**, 150901 (2019).
- M Hoffmann, et al., Deeptime: a python library for machine learning dynamical models from time series data. *Mach. Learn. Sci. Technol.* **3**, 015009 (2021).
- M Ghorbani, S Prasad, JB Klauda, BR Brooks, Graphvampnet, using graph neural networks and variational approach to markov processes for dynamical modeling of biomolecules. *The J. Chem. Phys.* **156**, 184103 (2022).
- S Banik, et al., Cegan: Crystal edge graph attention network for multiscale classification of materials environment (2022).
- RS Hong, et al., Insights into the polymorphic structures and enantiotropic layer-slip transition in paracetamol form iii from enhanced molecular dynamics. *Cryst. Growth & Des.* **21**, 886–896 (2021).
- RS DeFever, S Sarupria, Contour forward flux sampling: Sampling rare events along multiple collective variables. *The J. Chem. Phys.* **150**, 024103 (2019).
- C Velez-Vega, EE Borrero, FA Escobedo, Kinetics and mechanism of the unfolding native-to-loop transition of trp-cage in explicit solvent via optimized forward flux sampling simulations. *The J. Chem. Phys.* **133**, 105103 (2010).
- A Barducci, G Bussi, M Parrinello, Well-tempered metadynamics: A smoothly converging and tunable free-energy method. *Phys. Rev. Lett.* **100**, 020603 (2008).
- F Giberti, M Salvalaglio, M Parrinello, Metadynamics studies of crystal nucleation. *IUCrJ* **2**, 256–266 (2015).
- T Karmakar, M Invernizzi, V Rizzi, M Parrinello, Collective variables for the study of crystallization. *Mol. Phys.* **0**, e1893848 (2021).
- GC Sosso, et al., Crystal nucleation in liquids: Open questions and future challenges in molecular dynamics simulations. *Chem. reviews* **116**, 7078–7116 (2016).
- S Hussain, A Haji-Akbari, Studying rare events using forward-flux sampling: Recent breakthroughs and future outlook. *The J. Chem. Phys.* **152**, 060901 (2020).
- KE Blow, D Quigley, GC Sosso, The seven deadly sins: when computing crystal nucleation rates, the devil is in the details (2021).
- B Peters, BL Trout, Obtaining reaction coordinates by likelihood maximization. *The J. Chem. Phys.* **125**, 054108 (2006).
- A Ma, AR Dinner, Automatic method for identifying reaction coordinates in complex systems. *The J. Phys. Chem. B* **109**, 6769–6779 (2005).
- EE Borrero, FA Escobedo, Reaction coordinates and transition pathways of rare events via forward flux sampling. *The J. chemical physics* **127**, 164101 (2007).
- Z Zou, ST Tsai, P Tiwary, Toward automated sampling of polymorph nucleation and free energies with the sgoo and metadynamics. *The J. Phys. Chem. B* **125**, 13049–13056 (2021).
- CR Schwantes, VS Pande, Improvements in markov state model construction reveal many non-native interactions in the folding of nt19. *J. Chem. Theory Comput.* **9**, 2000–2009 (2013) PMID: 23750122.
- EE Borrero, FA Escobedo, Reaction coordinates and transition pathways of rare events via forward flux sampling. *The J. chemical physics* **127**, 164101 (2007).
- RS DeFever, S Sarupria, Nucleation mechanism of clathrate hydrates of water-soluble guest molecules. *The J. Chem. Phys.* **147**, 204503 (2017).
- NER Zimmermann, B Vorselaars, D Quigley, B Peters, Nucleation of nacl from aqueous solution: Critical sizes, ion-attachment kinetics, and rates. *J. Am. Chem. Soc.* **137**, 13352–13361 (2015).
- A Arjun, PG Bolhuis, Molecular understanding of homogeneous nucleation of co2 hydrates using transition path sampling. *The J. Phys. Chem. B* **125**, 338–349 (2021).
- LC Jacobson, M Matsumoto, V Molinero, Order parameters for the multistep crystallization of clathrate hydrates. *The J. Chem. Phys.* **135**, 074501 (2011).
- M Badin, R Martoňák, Nucleating a different coordination in a crystal under pressure: A study of the b1–b2 transition in nacl by metadynamics. *Phys. Rev. Lett.* **127**, 105701 (2021).
- D Wang, P Tiwary, State predictive information bottleneck. *The J. Chem. Phys.* **154**, 134111 (2021).
- S Mehdi, D Wang, S Pant, P Tiwary, Accelerating all-atom simulations and gaining mechanistic understanding of biophysical systems through state predictive information bottleneck. *J. Chem. Theory Comput.* **18**, 3231–3238 (2022).
- PR ten Wolde, D Frenkel, Computer simulation study of gas–liquid nucleation in a lennard-jones system. *J. Chem. Phys.* **109**, 9901–9918 (1998).
- PM Piaggi, O Valsson, M Parrinello, Enhancing entropy and enthalpy fluctuations to drive crystallization in atomistic simulations. *Phys. Rev. Lett.* **119**, 015701 (2017).
- PM Piaggi, M Parrinello, Predicting polymorphism in molecular crystals using orientational entropy. *Proc. Natl. Acad. Sci.* **115**, 10251–10256 (2018).
- PJ Steinhardt, DR Nelson, M Ronchetti, Bond-orientational order in liquids and glasses. *Phys. Rev. B* **28**, 784 (1983).
- P Tiwary, M Parrinello, A time-independent free energy estimator for metadynamics. *The J. Phys. Chem. B* **119**, 736–742 (2015).
- M Salvalaglio, P Tiwary, GM Maggioni, M Mazzotti, M Parrinello, Overcoming time scale and finite size limitations to compute nucleation rates from small scale well tempered metadynamics simulations. *The J. Chem. Phys.* **145**, 211925 (2016).
- KM Bal, Nucleation rates from small scale atomistic simulations and transition state theory. *The J. Chem. Phys.* **155**, 144111 (2021).
- D Moroni, PR ten Wolde, PG Bolhuis, Interplay between structure and size in a critical crystal nucleus. *Phys. Rev. Lett.* **94**, 235703 (2005).
- P Rein ten Wolde, MJ Ruiz-Montero, D Frenkel, Numerical calculation of the rate of crystal nucleation in a lennard-jones system at moderate undercooling. *The J. Chem. Phys.* **104**, 9932–9947 (1996).
- P Rein ten Wolde, D Frenkel, Homogeneous nucleation and the ostwald step rule. *Phys. Chem. Chem. Phys.* **1**, 2191–2196 (1999).
- I Volkov, M Cieplak, J Koplik, JR Banavar, Molecular dynamics simulations of crystallization of hard spheres. *Phys. Rev. E* **66**, 061401 (2002).
- S Auer, D Frenkel, Prediction of absolute crystal-nucleation rate in hard-sphere colloids. *Nature* **409**, 1020–1023 (2001).
- M Chopra, M Müller, JJ de Pablo, Order-parameter-based monte carlo simulation of crystallization. *The J. Chem. Phys.* **124**, 134102 (2006).
- C Desgranges, J Delhommelle, Molecular mechanism for the cross-nucleation between polymorphs. *J. Am. Chem. Soc.* **128**, 10368–10369 (2006).
- R Radhakrishnan, BL Trout, Nucleation of hexagonal ice (ih) in liquid water. *J. Am. Chem. Soc.* **125**, 7743–7747 (2003).
- R Radhakrishnan, BL Trout, Nucleation of crystalline phases of water in homogeneous and inhomogeneous environments. *Phys. Rev. Lett.* **90**, 158301 (2003).
- D Quigley, PM Rodger, Metadynamics simulations of ice nucleation and growth. *The J. Chem. Phys.* **128**, 154518 (2008).
- AV Brukhno, J Anwar, R Davidchack, R Handel, Challenges in molecular simulation of homogeneous ice nucleation. *J. Physics: Condens. Matter* **20**, 494243 (2008).
- A Reinhardt, JPK Doye, EG Noya, C Vega, Local order parameters for use in driving homogeneous ice nucleation with all-atom models of water. *The J. Chem. Phys.* **137**, 194504

- (2012).
73. W Lechner, C Dellago, Accurate determination of crystal structures based on averaged local bond order parameters. *The J. Chem. Phys.* **129**, 114707 (2008).
 74. PM Piaggi, M Parrinello, Calculation of phase diagrams in the multithermal-multibaric ensemble. *The J. Chem. Phys.* **150**, 244119 (2019).
 75. W Humphrey, A Dalke, K Schulten, Vmd: Visual molecular dynamics. *J. Mol. Graph.* **14**, 33–38 (1996).
 76. A Stukowski, Visualization and analysis of atomistic simulation data with OVITO-the Open Visualization Tool. *MODELLING AND SIMULATION IN MATERIALS SCIENCE AND ENGINEERING* **18** (2010).
 77. ER Beyerle, S Mehdi, P Tiwary, Quantifying energetic and entropic pathways in molecular systems. *The J. Phys. Chem. B* **126**, 3950–3960 (2022) PMID: 35605180.
 78. DP Kingma, M Welling, Auto-encoding variational bayes. *2nd Int. Conf. on Learn. Represent. ICLR 2014 - Conf. Track Proc.*, pp. 1–14 (2014).
 79. I Higgins, et al., beta-VAE: Learning basic visual concepts with a constrained variational framework in *International Conference on Learning Representations*. (2017).
 80. AA Alemi, I Fischer, JV Dillon, K Murphy, Deep variational information bottleneck. *CoRR abs/1612.00410* (2016).
 81. N Tishby, FC Pereira, W Bialek, The information bottleneck method (2000).
 82. F Noé, I Horenko, C Schütte, JC Smith, Hierarchical analysis of conformational dynamics in biomolecules: Transition networks of metastable states. *J. Chem. Phys.* **126**, 155102 (2007).
 83. P Deuflhard, W Huisinga, A Fischer, C Schütte, Identification of almost invariant aggregates in reversible nearly uncoupled Markov chains. *Linear Algebr. Its Appl.* **315**, 39–59 (2000).
 84. M Salvalaglio, C Perego, F Giberti, M Mazzotti, M Parrinello, Molecular-dynamics simulations of urea nucleation from aqueous solution. *Proc. Natl. Acad. Sci.* **112**, E6–E14 (2015).
 85. MJ Abraham, et al., Gromacs: High performance molecular simulations through multi-level parallelism from laptops to supercomputers. *SoftwareX* **1**, 19–25 (2015).
 86. GA Tribello, M Bonomi, D Branduardi, C Camilloni, G Bussi, Plumed 2: New feathers for an old bird. *Comp. Phys. Comm.* **185**, 604–613 (2014).
 87. M Bonomi, G Bussi, CC Camilloni, Promoting transparency and reproducibility in enhanced molecular simulations. *Nat. Methods.* **16**, 670–673 (2019).
 88. HP Weber, WG Marshall, V Dmitriev, High-pressure polymorphism in deuterated urea. *Acta Crystallogr. Sect. A* **58**, c174 (2002).
 89. FJ Lamelas, ZA Dreger, YM Gupta, Raman and x-ray scattering studies of high-pressure phases of urea. *The J. Phys. Chem. B* **109**, 8206–8215 (2005).
 90. A Olejniczak, K Ostrowska, A Katrusiak, H-bond breaking in high-pressure urea. *The J. Phys. Chem. C* **113**, 15761–15767 (2009).
 91. M Donnelly, et al., Urea and deuterium mixtures at high pressures. *The J. Chem. Phys.* **142**, 124503 (2015).
 92. K Dziubek, M Citroni, S Fanetti, AB Cairns, R Bini, High-pressure high-temperature structural properties of urea. *The J. Phys. Chem. C* **121**, 2380–2387 (2017).
 93. K Roszak, A Katrusiak, Giant anomalous strain between high-pressure phases and the mesomers of urea. *The J. Phys. Chem. C* **121**, 778–784 (2017).
 94. F Safari, M Tkacz, A Katrusiak, High-pressure sorption of hydrogen in urea. *The J. Phys. Chem. C* **125**, 7756–7762 (2021).
 95. F Giberti, M Salvalaglio, M Mazzotti, M Parrinello, Insight into the nucleation of urea crystals from the melt. *Chem. Eng. Sci.* **121**, 51–59 (2015).
 96. T Mandal, RG Larson, Nucleation of urea from aqueous solution: Structure, critical size, and rate. *The J. Chem. Phys.* **146**, 134501 (2017).
 97. NF Francia, LS Price, J Nyman, SL Price, M Salvalaglio, Systematic finite-temperature reduction of crystal energy landscapes. *Cryst. Growth & Des.* **20**, 6847–6862 (2020).
 98. C Shang, XJ Zhang, ZP Liu, Crystal phase transition of urea: what governs the reaction kinetics in molecular crystal phase transitions. *Phys. Chem. Chem. Phys.* **19**, 32125–32131 (2017).
 99. J Wang, RM Wolf, JW Caldwell, PA Kollman, DA Case, Development and testing of a general amber force field. *J. Comput. Chem.* **25**, 1157–1174 (2004).
 100. O Valskov, P Tiwary, M Parrinello, Enhancing important fluctuations: Rare events and metadynamics from a conceptual viewpoint. *Annu. review physical chemistry* **67**, 159–184 (2016).
 101. PG Vekilov, The two-step mechanism of nucleation of crystals in solution. *Nanoscale* **2**, 2346–2357 (2010).
 102. M Sleutel, J Lutsko, AE Van Driessche, MA Durán-Olivencia, D Maes, Observing classical nucleation theory at work by monitoring phase transitions with molecular precision. *Nat. Commun.* **5**, 5598 (2014).
 103. A Sauter, et al., On the question of two-step nucleation in protein crystallization. *Faraday Discuss.* **179**, 41–58 (2015).
 104. ND Loh, et al., Multistep nucleation of nanocrystals in aqueous solution. *Nat. Chem.* **9**, 77–82 (2017).
 105. FC Meldrum, RP Sear, Now you see them. *Science* **322**, 1802–1803 (2008).
 106. I Gimondi, M Salvalaglio, CO₂ packing polymorphism under confinement in cylindrical nanopores. *Mol. Syst. Des. Eng.* **3**, 243–252 (2018).
 107. GA Tribello, F Giberti, GC Sosso, M Salvalaglio, M Parrinello, Analyzing and driving cluster formation in atomistic simulations. *J. Chem. Theory Comput.* **13**, 1317–1327 (2017).
 108. DL Nelson, MM Cox, *Lehninger Principles of Biochemistry, Fifth Edition*. (Freeman), (2008).
 109. JW Lynch, Molecular structure and function of the glycine receptor chloride channel. *Physiol. Rev.* **84**, 1051–1095 (2004) PMID: 15383648.
 110. MA Razak, PS Begum, B Viswanath, S Rajagopal, Multifarious beneficial effect of nonessential amino acid, glycine: A review. *Oxidative Medicine Cell. Longev.* **2017**, 1716701 (2017).
 111. YG Bushuev, SV Davletbaeva, OI Koifman, Molecular dynamics simulations of aqueous glycine solutions. *Cryst. Eng. Comm.* **19**, 7197–7206 (2017).
 112. E Boldyreva, et al., Polymorphism of glycine, part i. *J. thermal analysis calorimetry* **73**, 409–418 (2003).
 113. Y Yani, PS Chow, RB Tan, Glycine open dimers in solution: New insights into α -glycine nucleation and growth. *Cryst. growth & design* **12**, 4771–4778 (2012).
 114. E Boldyreva, Glycine: The gift that keeps on giving. *Isr. J. Chem.* (2021).
 115. CL Bull, et al., ζ -Glycine: insight into the mechanism of a polymorphic phase transition. *IUCrJ* **4**, 569–574 (2017).
 116. S Prestipino, PV Giaquinta, The entropy multiparticle-correlation expansion for a mixture of spherical and elongated particles. *J. Stat. Mech. Theory Exp.* **2004**, P09008 (2004).
 117. A Baranyai, DJ Evans, Direct entropy calculation from computer simulation of liquids. *Phys. Rev. A* **40**, 3817–3822 (1989).
 118. Y Iitaka, The crystal structure of γ -glycine. *Acta Crystallogr.* **14**, 1–10 (1961).
 119. N Marom, et al., Many-body dispersion interactions in molecular crystal polymorphism. *Angewandte Chemie Int. Ed.* **52**, 6629–6632 (2013).
 120. N Duff, B Peters, Polymorph specific rmsd local order parameters for molecular crystals and nuclei: α -, β -, and γ -glycine. *The J. Chem. Phys.* **135**, 134101 (2011).
 121. Y Iitaka, The crystal structure of β -glycine. *Acta Crystallogr.* **13**, 35–45 (1960).
 122. A Dawson, et al., Effect of high pressure on the crystal structures of polymorphs of glycine. *Cryst. Growth & Des.* **5**, 1415–1427 (2005).
 123. RA Van Santen, The ostwald step rule. *The J. Phys. Chem.* **88**, 5768–5769 (1984).
 124. O Urquidí, J Brazard, N LeMessurier, L Simine, TBM Adachi, In situ optical spectroscopy of crystallization: One crystal nucleation at a time. *Proc. Natl. Acad. Sci.* **119**, e2122990119 (2022).
 125. A Bouchard, GW Hofland, GJ Witkamp, Solubility of glycine polymorphs and recrystallization of β -glycine. *J. Chem. & Eng. Data* **52**, 1626–1629 (2007).
 126. C Parks, et al., Solubility curves and nucleation rates from molecular dynamics for polymorph prediction – moving beyond lattice energy minimization. *Phys. Chem. Chem. Phys.* **19**, 5285–5295 (2017).
 127. T Karmakar, PM Piaggi, M Parrinello, Molecular dynamics simulations of crystal nucleation from solution at constant chemical potential. *J. Chem. Theory Comput.* **15**, 6923–6930 (2019) PMID: 31657927.
 128. Y Wang, JML Ribeiro, P Tiwary, Past-future information bottleneck for sampling molecular reaction coordinate simultaneously with thermodynamics and kinetics. *Nat. communications* **10**, 1–8 (2019).
 129. WL Jorgensen, J Chandrasekhar, JD Madura, RW Impey, ML Klein, Comparison of simple potential functions for simulating liquid water. *The J. Chem. Phys.* **79**, 926–935 (1983).
 130. DA Case, et al., The amber biomolecular simulation programs. *J. Comput. Chem.* **26**, 1668–1688 (2005).
 131. YG Bushuev, SV Davletbaeva, OI Koifman, Molecular dynamics simulations of aqueous glycine solutions. *CrystEngComm* **19**, 7197–7206 (2017).
 132. HJC Berendsen, JR Grigera, TP Straatsma, The missing term in effective pair potentials. *The J. Phys. Chem.* **91**, 6269–6271 (1987).
 133. JL Derissen, PH Smit, J Voogd, Calculation of the electrostatic lattice energies of α -, β -, and γ -glycine. *The J. Phys. Chem.* **81**, 1474–1476 (1977).
 134. DW Cheong, YD Boon, Comparative study of force fields for molecular dynamics simulations of α -glycine crystal growth from solution. *Cryst. growth & design* **10**, 5146–5158 (2010).
 135. H Jiang, PG Debenedetti, AZ Panagiotopoulos, Nucleation in aqueous nacl solutions shifts from 1-step to 2-step mechanism on crossing the spinodal. *The J. Chem. Phys.* **150**, 124502 (2019).
 136. G Bussi, D Donadio, M Parrinello, Canonical sampling through velocity rescaling. *J. Chem. Phys.* **126**, 014101 (2007).
 137. M Parrinello, A Rahman, Polymorphic transitions in single crystals: A new molecular dynamics method. *J. Appl. physics* **52**, 7182–7190 (1981).
 138. U Essmann, L Perera, ML Berkowitz, A smooth particle mesh ewald method. *J. Chem. Phys.* **103**, 8577–8593 (1995).
 139. B Hess, P-lincs: a parallel linear constraint solver for molecular simulation. *J. Chem. Theory* **4**, 116–122 (2007).
 140. U Groemping, Relative importance for linear regression in r: The package relaimpo. *J. Stat. Softw.* **17**, 1–27 (2006).
 141. J Towns, et al., Xsede: Accelerating scientific discovery. *Comput. Sci. Eng.* **16**, 62–74 (2014).